PHASE-SEPARATION OF WETTING FLUIDS USING NANOPOROUS ALUMINA MEMBRANES AND MICRO-GLASS CAPILLARIES

Damena D. Agonafer, Ken Lopez, Yoonjin Won, James Palko, Mehdi Asheghi, Juan G. Santiago, Kenneth E. Goodson
Stanford University
Mechanical Engineering Department
440 Escondido Mall
Stanford, CA, USA, 94305
Email: agonafer@stanford.edu

ABSTRACT

Phase separation in two-phase microfluidic exchangers is a promising strategy for reducing the required pumping power. Past research has focused on using hydrophobic nanoporous structures in order to extract water vapor and retain liquid within the vapor-cooling device. This study focuses on characterizing the bursting pressure, the maximum Laplace pressure for liquid containment, of nanoporous alumina membranes and micro-glass capillaries. The pore size diameters of the alumina membranes have a nominal diameter of 170 nm that can produce a pressure drop of 1.5 kPa for wetting dielectric liquids. In order to contain higher Laplace pressures, the pore geometry for 'pinning' of the fluid at the liquid-vapor interface needs to be optimized. Single glass micro-glass capillaries were used in order to study the 'pinning effect' of wetting fluids for various micro-capillary diameters. The glass capillary diameters ranged from 250-840 µm with measured Laplace pressures up to ~0.9 kPa. Experimental results agreed well with an analytical model that calculates the Laplace pressure as a function of pore geometry.

KEYWORDS: Two-Phase Evaporative Cooling, Microfluidics, Interfacial Nanoscale Transport, High-Heat Flux Electronic Applications, Burst Pressure Physics

NOMENCLATURE

Ca	capillary number
d	capillary outer diameter, m
h	spacing parameter, m
P	pressure, Pa
R	radius of curvature of meniscus, m
r	radius of curvature of pore edge, m
v	liquid front velocity, m/s

Greek Symbols

α	angle of sharpness (°)
β	meniscus curvature center-point angle (°)
δ	pore spacing (m)
γ	surface tension (N/m)
φ	characteristic tracking angle (°)
μ	dynamic viscosity (Pa*s)
θ	equilibrium contact angle (°)
ω	angle of expansion (°)

Subscripts

NW	non-wetting
W	wetting

INTRODUCTION

The rapid growth in transistor density in microprocessors has been accompanied by increases in power density. The heat flux for high performance chips in the 14 nm generation is projected to be greater than 100 W/cm^2 with a junction-to-ambient thermal resistance <0.2°C/W [1]. In addition, the "More-than-Moore (MTM)" paradigm such as 3D Packaging has thermal challenges distinct from that due to transistor scaling [2]. Reliability challenges resulting from coefficient of thermal expansion (CTE) mismatches as well as silicon efficiency reduction due to keep-out-zones when using Through Silicon Via (TSV) makes it a multi-disciplinary problem [3, 4]. High power density GaN HEMT technology can increase the capability of defense electronics systems with the reduction of CSWaP. However, thermal limitations have currently prevented the inherent capabilities of this technology where transistor-level power densities that exceed 10 kW/cm^2 are electrically feasible. This has motivated research on liquid cooling, both direct [5] and indirect [6], have been well with an emphasis on addressing challenges for high power electronics and reducing cost related to the system level integration.

One of the major challenges with microfluidics cooling strategies has been reducing pressure drop and pumping power requirements, where much effort has been invested in advanced fluid routing and manifolding methodologies that decrease pressure drop for single-phase flow and improve stability for two-phase flows [7, 8]. The fluid routing challenge was addressed through tree-like or fractal-derived networks [9, 10] or through distributed chip-normal manifolding [11]. Several patents feature distributed, chip-normal fluid routing to a microfluidic heat exchange region [12, 13], which could take the form of either microchannels, distributed microscale pin fins, or microporous foam structures. Additional research has focused on investigation of non-uniform allocation of micro-channels and for a given cooling design were able to show considerable reduction in pumping power requirements in contrast to conventional uniform micro-channel approaches [14].

Two-phase flow is promising for reducing pumping power requirements, but convection in microchannels can introduce Ledinegg instabilities, flow regime oscillation, and dryout/hotspots [15-17]. Nanoengineered structures and surfaces that can be integrated into liquid-vapor phase change systems have fundamentally transformed the design of two-phase microcooling heat exchangers. David et *al*. [8] demonstrated vapor extraction through a nanoporous hydrophobic PTFE coated nanoporous membrane that focused

on mitigation of thermal and hydrodynamic resistances. Thin-layer evaporative cooling devices integrated with nanoporous alumina structures have achieved heat removal up to 600 W/cm^2 [18]. Nanostructured surfaces may change the wetting characteristics and potentially enhance transport phenomena at micro/nano scales. Superhydrophobic surfaces [19], hydrophobic-hydrophilic patterns [20], and the use of micro/nanoengineered features [21] can promote spontaneous bubble removal and assist heat removal from the surface. Wang et *al.* [22] studied nanostructured surfaces to control fluidic behavior and enhance heat dissipation in microfluidic systems. Continued attention to nanoengineered surface features is expected to continue the trends to higher heat fluxes and improved stability. In this work, burst pressure experiments are done for wetting liquids in order to understand the mechanism for phase separation. These fundamental studies will aid in designing a bilayer phase separator for a microcooling heat exchanger. The role of the bilayer is to hold a burst pressure that is larger than the viscous pressure loss across a conductive microporous liquid delivery layer. Recently, two-phase microfluidic devices have been demonstrated with porous membrane structures to vent vapor bubbles from unobstructed flow channels and separate the liquid-vapor interface without flooding of the membrane surface [8, 24] However, these devices use water as a working fluid with hydrophobic porous structures, which can retain liquid at high working pressures (*i.e.*, exhibit high bursting pressures) while keeping the porous membrane dry. The current study involves the use of highly wetting liquids (*i.e.*, refrigerants) for two-phase cooling, which presents a challenge in designing a membrane that exhibits reasonable liquid burst pressures. For wetting solid-liquid-air interfaces (*i.e.*, bare solid surfaces with liquid contact angles $\theta < 90°$) the sole mechanism for which liquid retention is obtained (*i.e.* positive bursting pressures) is through the effective "pinning" of the liquid meniscus at sharp discontinuities along the solid surface [25]. For such discontinuities, there is a wide range of equilibrium angles that can exist at the three-phase contact line at the very edge [26, 27]. Thus, the fluid can have a range of stability angles at the edge that can produce positive pressures, which will be discussed in further detail in the modeling section.

Many applications of liquid pinning have been applied in areas such as designing hierarchical micro-nano patterned superhydrophobic [28-30] and superoleophobic surfaces (*i.e.*, surfaces that repel low surface tension fluids such as alkanes) [31-33]. Since there are no naturally occurring superoleophobic surfaces, unlike superhydrophobic surfaces, these wetting interfaces need to be designed properly via appropriate surface patterning and roughness [33]. The goal of effective pinning for low surface tension liquids is to ensure that the energy barrier, which separates the unfavorable non-wetting Metastable state from the more favorable fully-wetting Wenzel state, is large enough to achieve effective locking of the liquid in the non-wetting state [34]. The pinning phenomenon on structured surfaces has provided insight on the design of a porous membrane with high bursting pressure for highly wetting fluids. Another applicable study on pinning involves the use of microcapillary stop valves for restricting flow in microchannels via the sudden expansion of the microchannel [35-37]. Rapid enlargement of the microchannel changes the physical angle between the liquid interface and the solid interface, which forms a temporary barrier for the advancing liquid. For wetting solid-liquid interfaces, the expansion angle must be much larger (*i.e.*, must have a sharper microchannel outlet) for the device to exhibit adequate bursting pressures [38-40]. In a more recent study, Berthier *et al*. [39, 40] presented a model for pinning the working liquid, water, along sharp-edged microposts while water flowed through a microchannel.

To the authors' knowledge, this paper represents the first study on burst pressure measurements across micro/nano-porous structures for dielectric liquids. The present study will demonstrate how liquid pinning of wetting fluids can be achieved by expanding/sharp pores. Pinning the liquid at the pore edge can provide a means of enhancing the burst pressure characteristics for the bilayer phase separator. To understand the liquid pinning behavior and its potential impact on bursting pressure for wetting fluids, sharp glass capillary tubes of varying sizes were used in this study. The bursting pressure is measured using a pressure transducer that is set along a flow line to a pressure cell with a viewing window for simultaneous recording by a CCD camera.

EXPERIMENTAL SETUP & PROCEDURE

Bursting Pressure Apparatus

Initial bursting pressure experiments were done on commercially purchased alumina (Al_2O_3) membranes (Whatman Anopore), which were used for their uniformity in pore size distribution and simple geometry. The goals of the Al_2O_3 membrane experiments were to visualize and study the conditions of bursting through the membranes. To validate the burst pressure measurements, an optical microscope (Nikon Eclipse 80i), with 5x magnification, was used to visualize the bursting event through the Al_2O_3 membrane while being simultaneously recorded with a CCD camera (Thorlabs DCC1545M) as shown in Figure 1. The setup contains a programmable syringe pump (Harvard PHD 2000) for pumping the fluid connected in series with a pressure transducer (Omega PX419), with 0-5 psig range. A T-junction with a capillary tube of 177 μm inner diameter (ID) was placed before the cell and submerged in an elevated liquid reservoir in order to avoid any capillary back pressure formed by droplets at the capillary tube tip. The burst pressure cell is designed to clamp the Al_2O_3 membrane onto the cell itself while liquid penetration through the Al_2O_3 is visualized (Figure 2). The experimental procedures are explained in the latter.

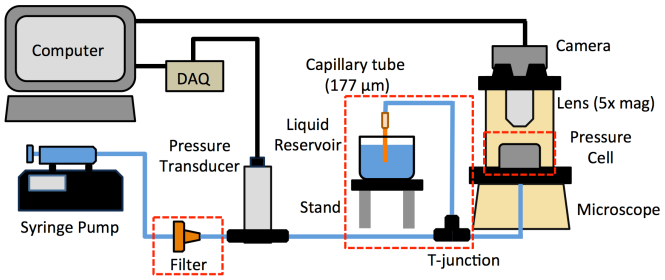

Fig 1: Apparatus for visualization and pressure measurements for burst pressure experiments.

The second set of experiments that were explored involved understanding the mechanism of pinning and its effect on bursting pressure by the use of micro-glass capillaries (VitroCom). A similar apparatus was used for the glass capillary bursting pressure experiments but without the presence of a T-junction and membrane filter (marked by the dotted red lines on the schematic in Figure 1). Furthermore, instead of utilizing the pressure cell, the glass capillaries were mounted on a small clamping stand. Objective lenses of 5x and 10x magnification were used. The burst pressure event was characterized by observation of a maximum pressure followed by either a sudden pressure drop or steady state plateau depending on the characteristic of the fluid.

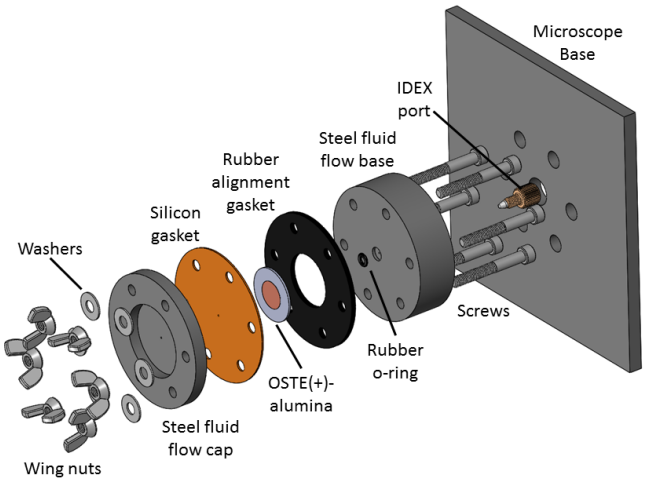

Fig 2: An exploded schematic of the burst pressure cell. To prevent leakage, the Al_2O_3 membrane is bonded to a polymer adhesive and sandwiched between silicon and rubber gaskets.

Alumina-OSTE(+) Sample Preparation

In order to prevent leakage around the Al_2O_3 membranes, the membrane was integrated into a polymer adhesive, off-stoichiometry-thiol-ene-epoxy (OSTE(+)) (Mercene Labs). The steps for fabricating the OSTE(+)-Al_2O_3 membranes are summarized in Figure 3. A Teflon mold was first fabricated in order to prevent any OSTE(+) polymer from adhering to the mold for easy removal. A pin of 1/32 in outside diameter (OD) was placed in the mold to allow for a liquid flow path through the membrane. The OSTE(+) polymer mix was poured into the mold and set underneath a UV lamp for 4 minutes. The UV-cured OSTE(+) mold was now flexible, workable, but still strongly adhesive. The UV-cured OSTE(+) mold was placed on a piece of Teflon and the membrane was dropped and lightly pressed onto the OSTE(+) mold. Another piece of Teflon was placed on top of the membrane along with a weight of 10 grams. This was placed in the oven for 1 hour at 70°C. The oven cure allows the membrane to completely adhere onto the OSTE(+), which hardens in the process.

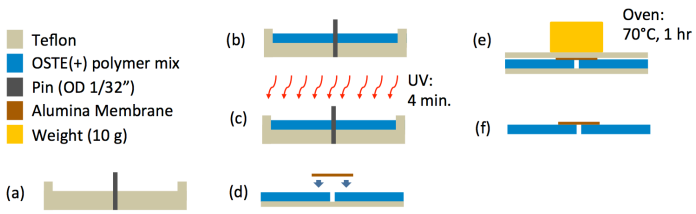

Fig 3: Fabrication procedure for bonding a polymer OSTE(+) gasket to an alumina membrane.

Experimental Procedures

All Al_2O_3 membrane bursting pressure experiments were conducted using the same procedure and conditions. The syringe pump was programmed to pause for an initial 2 minutes in order to capture the initial steady-state pressure. At the 2-minute mark, the flow rate was set to perform a ramping flow: the flow increased by an increment of 0.5 µl/min every 1 second. This allows the system pressure to increase while the fluid flows through the Capillary tube at the T-junction. This T-junction allows the ejection of gas bubbles in the line and prohibits any air in the system to be compressed as the pressure rises, which may diminish the visual readout of the burst pressure location in the pressure data curve.

The ramping flow continues for the duration of the experiments, even after the bursting event occurs. The pressure data is recorded using a DAQ-LabView setup simultaneously with the video recording. In the results, the time at which the burst happens in the video is matched with the time at which an inflection point is seen in the pressure data curve; this will be further discussed in the results section.

In the glass capillary experiments, the syringe was programmed to pause initially for 1 minute and then flow at a constant flow rate for the duration of the experiment. The flow rates used satisfied the capillary flow regime defined by the capillary number:

$$Ca = \frac{\mu v}{\gamma} \quad (1)$$

, where μ is the dynamic viscosity, v is the liquid front velocity, and γ is the surface tension. In order to achieve capillary-driven flow, the capillary number must be $\leq 10^{-5}$, which was satisfied in all experiments. The pressure data collection ran simultaneously with the video recording. A characteristic peak was captured from the pressure data and matched with the video recording. Table 1 summarizes the fluids and their properties [41, 42] used for both sets of experiments.

Table 1: Liquid properties four fluids used for bursting pressure experiments.

	Dynamic Viscosity (mPa*sec)	Surface Tension (N/m)	Contact angle w/glass
Water	0.890	0.072	~ 60°
IPA	1.96	0.0214	~ 0°
FC-40	4.1	0.016	~ 0°
HT-170	3.2	0.018	~ 0°

Characterization of Nanoporous Alumina Membrane and Glass Micro-Capillary

The purpose of the image analysis is to estimate the pore sizes of Al_2O_3 membranes in order to provide input to the bursting pressure calculations. The Al_2O_3 membrane samples are first cleaved to gain visual access from the top and side views. All images are taken using a FEI XL30 Sirion Scanning electron microscope (SEM). The image process starts with cropping the SEM images (Fig. 4a) and binaries to convert grey image to black and white images (Fig. 4b). The morphological erode and dilate processing are performed to remove small objects from an image while preserving the shape and size of larger objects in the image (Fig. 4c). By computing connected components for binary images (white segment), the location, area, and diameter of each pore are obtained. The average of pore diameter is 150 nm with a standard deviation of 20 nm from the top view. For a side view image, 50 evenly spaced probe lines are drawn (Fig. 5). The intersections between these lines and the pores are counted in the horizontal to calculate the pore diameters. The side view images show a deviation of 70 nm. Table 2 summarizes the Al_2O_3 membrane geometrical parameters based on the SEM image analysis.

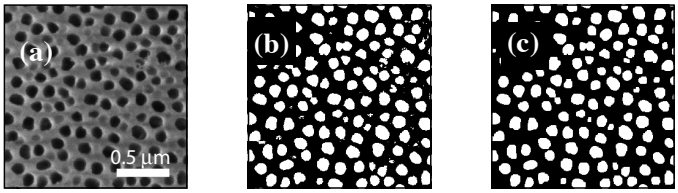

Fig 4: (a) An SEM of an Al_2O_3 membrane from a top view. (b) The binary image after filtering. (c) The image after post-processing.

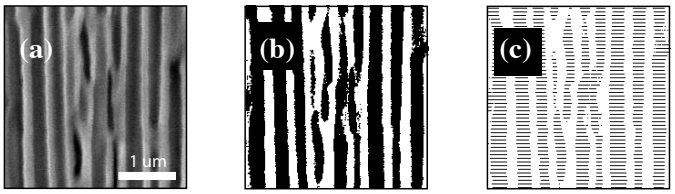

Fig 5: (a) An SEM of an Al_2O_3 membrane from a side view. (b) The binary image after filtering. (c) Horizontal straight probe lines drawn across the binary image to detect intersections with pores.

Table 2: Resulting parameters using image analysis.

Parameter	Value
Nominal Pore Diameter	150 nm
Pore Size Distribution across the Plane	15 nm
Pore Diameter Variation along the Pores	70 nm
Porosity	35 %

MODELING THE PINNING EFFECT

Parametric Study of Geometric Configurations

The goal of the analytical studies are to find a membrane pore geometry that can produce large Laplace bursting pressures by means of pinning at the pore outlet. To simplify physics and geometry, for potential microfabrication, a single rounded-edge pore geometry with an expansion angle, ω, was modeled. The geometry exhibits three main parameters: edge angle sharpness, α (where α=180°-ω), edge radius of curvature, *r*, and pore diameter, δ. The schematic in Figure 6 depicts the pore geometry used for the parametric study. This model only considers surface tension effects (*i.e.*, capillary flow). The model and the following derivation were modified from a previous study on pinning on microposts in Berthier *et al.*[38].

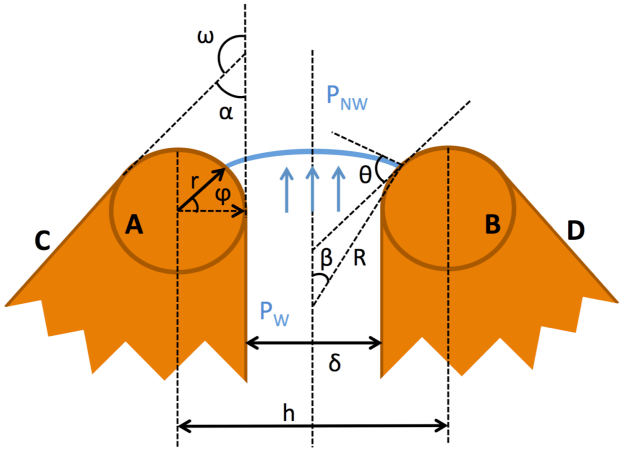

Fig 6: Schematic of rounded-edge pore model for single pore.

The meniscus has a radius of curvature, *R,* that is defined at each characteristic tracking angle, φ, along the rounded edge with radius of curvature *r,* defined as:

$$R(\varphi) = \frac{\frac{h}{2} - r\sin\left(\frac{\pi}{2} - \varphi\right)}{\sin(\beta)} \qquad (2)$$

, where β is a meniscus curvature center-point angle ($\beta=\theta-\pi/2+\varphi$), h is a spacing parameter ($h=2r+\delta$) and θ is the equilibrium contact angle of the fluid with the solid interface (for simplification, equilibrium contact angle is used instead of advancing angle). In the model, the meniscus travels in steps of φ all along the circular edges, labeled A and B, symmetrically about the middle. At each point in φ the fluid is at the equilibrium contact angle θ with the solid interface, satisfying capillary flow.

The radius of curvature of the meniscus, R, is minimized in order to yield a maximum possible capillary pressure, ΔP_{max}, defined by Young-Laplace:

$$\frac{dR(\varphi)}{d\varphi} = 0 \rightarrow \varphi_{min} \rightarrow R_{min} \quad (3)$$

$$\varphi_{min} = -\sin^{-1}\left(\frac{2\,r\sin(\theta)}{h}\right) - \theta + \pi \quad (4)$$

$$\Delta P_{max} = P_{NW} - P_W = \frac{2\gamma}{R_{min}} \quad (5)$$

, where P_{NW} is the pressure at the non-wetting side and P_W is the pressure at the wetting side. The bursting pressure, defined as the maximum pressure at which the meniscus becomes unstable, is achieved by one of the following criteria: 1. If the location of the minimum radius of curvature, φ_{min}, is ≤ 180°- α then the bursting pressure occurs due to the minimum radius of curvature, 2. If φ_{min} ≥ 180°- α, the bursting pressure occurs due to the meniscus reaching the next surface defined by C and D in Figure 6.

The analytical burst pressure model was implemented into MATLAB for a parametric study involving the geometric parameters α, r, and δ. Figure 7 depicts the results of the parametric study for dielectric fluid FC-40 with a contact angle of 0° and surface tension 0.016 N/m.

The parametric study suggests that at smaller angles of sharpness, α, larger burst pressures are possible. The radius of curvature of the pore edge, r, also has a significant impact on the bursting pressure. A very small radius of curvature at the edges, relative to the pore spacing δ, provides higher burst pressures by a factor of 2, compared to a larger radius of curvature. It can be conclude that "pinning" can produce high bursting pressures for fluids with low surfaces tension, including dielectrics.

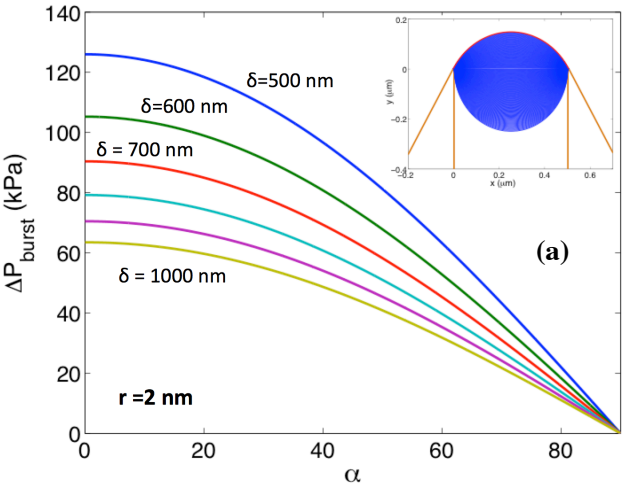

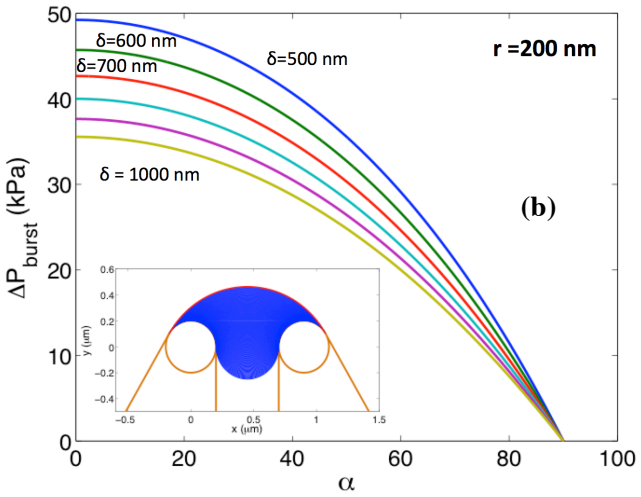

Fig 7: Parametric study of burst pressure model. The results show bursting pressure results for varying pore sizes, δ, represented by each different color curve as a function of pore edge angle, α. The inset images portray the size of the radius of curvature of the edge, r, compared to δ of 500 nm with an α of 30° as fluid travels through the pore. (a) The r of 2 nm is orders of magnitude smaller than the pore spacing δ, which gives a sharper defined edge. (b) When r, of 200 nm, is in the same order of magnitude as the pore spacing, δ, the pressures are smaller, by approximately a factor of 2.

Experimental Glass Capillary Model

In order to validate the glass capillary experiments, an experimental glass capillary model for bursting pressure was derived. This model captures the meniscus of a fluid at the outer edge of a glass capillary tube and its corresponding pressure; therefore pressure due to the inner diameter is not considered in this model. Figure 8 shows a schematic of the glass capillary model along the outer diameter. The primary geometric parameters that this model exhibits are: capillary OD, d, and edge radius of curvature, r.

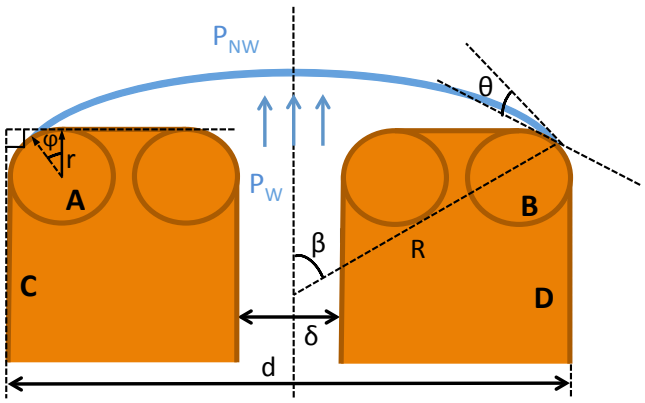

Fig 8: Schematic of glass capillary model for outer diameter of tube defined by d.

Like the previous model, this experimental model tracks the meniscus with radius of curvature R as it travels along the edge with curvature r at each defined step φ. The meniscus radius of curvature is defined as:

$$R(\varphi) = \frac{r\sin(\varphi) + \frac{d}{2} - r}{\sin(\beta)} \quad (6)$$

$$\varphi_{min} = \cos^{-1}\left(\frac{2\,r\sin(\theta)}{d - 2\,r}\right) - \theta \quad (7)$$

, where $\beta=\theta+\varphi$. The same procedure for minimizing the radius of curvature was done to find the maximum possible capillary pressure. Likewise, there are two bursting criteria: 1. If the location of the minimum radius of curvature, φ_{min}, is ≤ 90° then the bursting pressure occurs due to the minimum radius of curvature, 2. If φ_{min} ≥ 90°, the bursting pressure occurs due to the meniscus reaching the next surface defined by C and D in the schematic.

The model was implemented in MATLAB by applying the analytical solution of the meniscus radius of curvature as a function of location, $R(\varphi)$, with the two bursting criteria presented. Figure 9 shows the model during capillary-driven flow at the rounded edge interface using FC-40 and water, respectively, for a capillary tube with an OD, d, of 550 μm and ID of 400 μm. In Figure 9a,c the meniscus of the fluid is depicted at each location along the edge of the pore opening, φ, in real-time. Simultaneously, the capillary pressure at each location φ is indicated on the pressure plot in Figure 9b,d. Once one or both of bursting pressure criteria is satisfied, the result indicates the location and value of the maximum pressure. For this case the radius of curvature of the edge, r, is 1 μm ($r << d$) and the number of steps in φ is 10.

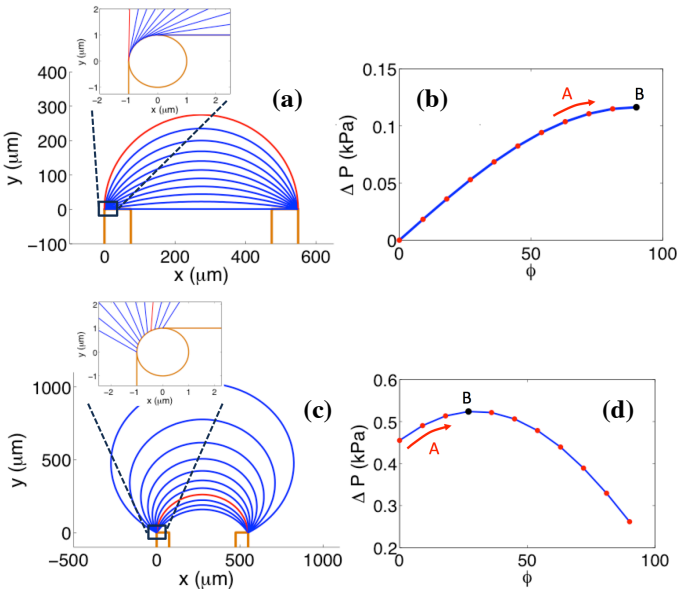

Fig 9: Real-time result of capillary flows along the OD of the glass capillary of 550 μm for FC-40 and water, respectively. (a,c) Meniscus capillary flow at each location φ along the OD. The red line indicates the meniscus location at burst. (b,d) Capillary pressure at each location φ. Along A the meniscus pressure is increasing until it reaches point B where bursting occurs.

In the FC-40 results the meniscus of the fluid, R, reaches a bursting pressure at 0.116 kPa. The location of burst is at φ=90°, which means that the burst event occurred due to both criteria. The meniscus achieved its minimum radius of curvature and reached the surfaces C and D indicated in Figure 8. Since the contact angle for FC-40 on glass is ~0°, the bursting will occur due to both criteria for the glass capillary used in the experiments for all OD sizes. The same goes for isopropanol, which has a contact angle with glass of ~0°. For water, of contact angle 60°, the results will only satisfy the first criteria since the fluid meniscus reaches its minimum radius of curvature before reaching the outside capillary walls. From the results we can see that water obtained its maximum pressure at 0.525 kPa at a location of φ=27°. This means that the burst pressure occurred before the fluid reached the surface of the outer diameter, defined in Figure 8 as surfaces C and D. Even though the radius of curvature of the water meniscus, R, reaches a minimum, there's still a finite distance for liquid to flow along the edge radius of curvature, r. The pressures due to the continued growth past the bursting pressure are lower as the radius of curvature, R, decreases and the droplet expands in size.

RESULTS AND DISCUSSION

Bursting Pressure Results for Nanoporous Alumina Membrane

Figure 10 shows pressure traces for the flow of several fluids through the nanoporous alumina membranes. A key result from these traces is the lack of a clear pressure signature of burst. Penetration of liquid through the membrane is marked by plateaus and changes in slope. We attribute the features of the pressure trace to differing membrane permeability and viscosity for air versus liquid as well as geometry of the dead volume in the system. The period marked A is prior to the ramping flowrate and is attributed to the hydrostatic pressure of the system. Period B corresponds to the filling of liquid in the parallel paths of the capillary tubes leading to the microcapillary and burst pressure cell. The increase in pressure can be attributed to viscous resistance as flow rate increases and a larger length of the capillary is wetted. We believe the plateau observed following period B for some liquids is the result of filling dead space below the membrane in the sample cell, based on the flow volumes and timing corresponding to the plateau. Up to this point, the membrane remains dry, and only air is forced through it. At point C, the membrane is wetted and liquid appears on the top surface. Period D corresponds to viscous liquid flow through the membrane with pressure increasing as the flow rate increases. At all times, flow through the T-junction to the reservoir is active providing a parallel flow path and viscous resistance. The observed pressure traces result from the addition in parallel of the reservoir bypass and the membrane flow resistances.

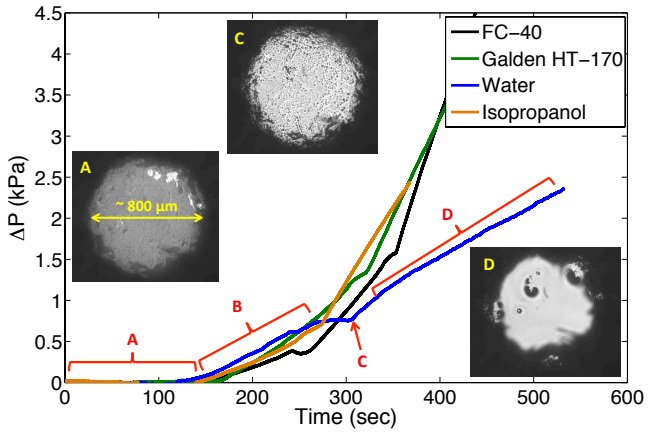

Fig 10: Bursting Pressure Results for Water, Isopropanol, FC-40, and Galden HT-170 through Al_2O_3 with an average pore diameter of 1

Table 3: Bursting Pressure Results for Al_2O_3 Membranes

	Initial Slope (kPa/sec)	Final Slope (kPa/sec)	Inflection Pressure (kPa)
Water	0.00572	0.00653	1.036±0.331
IPA	0.00491	0.0183	0.834±0.190
FC-40	0.0133	0.0339	1.436±0.288
HT-170	0.00807	0.0238	1.392±0.190

The initial slopes of all fluids are reasonably close in value (Table 3). This could be attributed to the dominant contribution of expelling air from the system. After the bursting event occurs through the Al_2O_3 membrane, the ratio of slopes of each fluid are nearly proportional to the viscosity. Additional factors such as surface tension and evaporative effects of the fluid could also influence the rate of pressure increase. Burst pressure experiments for Al_2O_3 membranes with a nominal pore size of 150 nm demonstrate their inability to sustain any significant busting pressures as required for the evaporative microcooling device under consideration. The results are consistent with the analytical results from the rounded-edge pore model in Figure 6, which shows that for an edge angle sharpness α=90°, the capillary pressure is zero. It is therefore important to look at geometrically optimized pore structures in order to pin the fluid.

Bursting Pressure Results for Glass Capillaries

Figure 11 shows pressure traces of flow through various size capillaries for DI water, IPA, and FC-40. These plots correspond to constant flow rate experiments and show the expected signature of burst, a discernible drop in pressure or prolonged plateau. All plots are referenced to the ambient pressure before flow starts. Initially flow encounters minimal viscous effects as the flow rate is maintained well below the regime where viscous effects are significant ($Ca<10^{-5}$), and consequently, the pressure remains constant. During this period, the pressure in the liquid is lower than that in the gas above by an amount determined by the curvature of the meniscus as it climbs up the capillary. When the meniscus reaches the top of the capillary, it becomes "pinned" on the inner edge, as shown at point B for IPA in Figure 11b. At this point the pressure in the liquid begins to rise as the meniscus becomes less concave. Eventually, the meniscus becomes planar, and the pressure between the liquid and gas phases is equal. The pressure change corresponding to this equalization, calculated based on the capillary ID, liquid surface tension, and equilibrium contact angle is indicated by horizontal dotted lines in the figures.

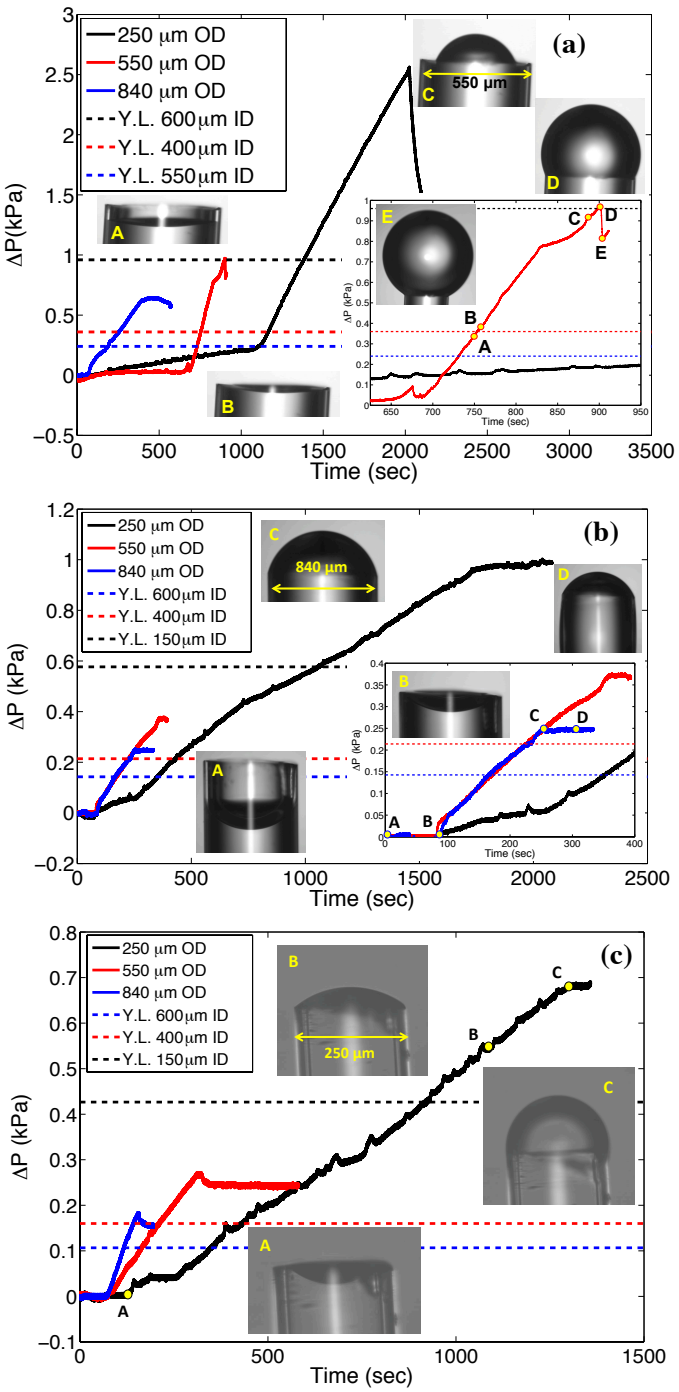

Fig 11: Glass capillary bursting pressure experimental results

for (a) water, (b) IPA, (c) FC-40. The contributions of capillary pressure from the inner diameter are calculated using the Young-Laplace equation (Y.L.).

As flow continues, the meniscus becomes convex, and the pressure of the liquid rises above that of the gas. The meniscus may remain pinned at the inner edge of the capillary for a time, as seen for water in Figure 11a, point C[1]. Further flow drives increasing curvature of the meniscus until the advancing contact angle with respect to the base of the capillary is reached. At this point, the meniscus "runs" to the outer edge of the capillary and again becomes pinned. Further flow increases the curvature of the meniscus until it forms its equilibrium contact angle with the outer surface. For water, the minimum radius of curvature is at φ=27°, which occurs before it reaches equilibrium with the outer micro-capillary surface. For FC-40 and IPA, the minimum radius of curvature at φ =90°, coincides with an angle of 180° with the outer capillary surface. At this point the pressure achieves a maximum, shown in point D in Figure 11a. Any further increase in volume under the meniscus reduces the curvature. The behavior of the pressure with increased flow beyond the maximum pressure point depends on the character of the liquid. Water, having high surface tension, forms an expanding droplet whose increasing radius of curvature results in a noticeable drop in pressure, as seen by point E in Figure 11a.

The pressure curve for water is different from IPA and FC-40 due to the difference of equilibrium contact angle and vapor pressure for each fluid. The contact angle for water is ~60°, which means that a convex meniscus can be formed with the water pinned at the inner edge of the microcapillary. Further flow increases the curvature until the advancing contact angle with respect to the flat end surface of the capillary is reached. At this instant, the water will move from the inner edge to the outer edge. Again water will pin at the outer edge and Laplace pressure and curvature increase with further flow. Curvature reaches a maximum when the meniscus is a hemisphere (i.e. equilibrium contact angle with the outer edge is ~0°). Further flow beyond this point results in a reduction of the Laplace pressure, but water will not advance down the sides of the capillary until the advancing contact angle (~60°) is reached. Therefore, the pressure vs. flow curves for water shows a distinct maximum. For FC-40 and IPA, the equilibrium contact angle (~0°) is reached at the instant the liquid interfaces with the top surface of the microcapillary. The meniscus immediately advances to the outer edge. The inner edge cannot hold a positive meniscus for a completely wetting liquid. Furthermore, as opposed to water, which pins at the outer edge of the capillary as the meniscus expands beyond a hemisphere and the meniscus curvature and Laplace pressure decrease, lower surface tension liquids, such as IPA and FC-40, "run" along the outer edges of the capillary as soon as the meniscus reaches a contact angle of ~0° with the outer surface (i.e. the meniscus forms a hemisphere), as can be noted in Figure 11b point D. The point at which the meniscus advances along the outer capillary wall coincides with the maximum Laplace pressure. The pressure reaches a plateau as the curvature of the meniscus achieves a steady state balancing the viscous flow along the outer capillary surface and the evaporation of the liquid.

The shape of the pressure/flow curve after burst is influenced by quasi-static and dynamic effects and depends on the specific properties of the liquid and the flow rate. Neglecting dynamic effects, liquids with a contact angle larger than zero would be expected to show a distinct maximum in pressure as the meniscus is pinned at the outer edge of the capillary and expands beyond a hemisphere (at which Laplace pressure is maximized), whereas liquids with contact angle of zero run along the outer edge of the capillary when the meniscus reaches a hemispherical shape and would be expected to show a plateau in the pressure/flow curve following burst. Dynamic effects, however, also have a strong effect on the pressure/flow behavior. At steady state, flow up the capillary is balanced by evaporation from the surface of the liquid streaming down the sides of the capillary and the meniscus itself (and possibly by liquid streaming off the capillary completely). The rate of evaporation increases with vapor pressure for a given surface area. The rate of streaming down the side of the capillary, exposing additional surface area for evaporation, increases with wetting strength of the liquid and decreases with viscosity. For higher flow rates, the balance of evaporation and capillary flow can result in a meniscus with radius larger than a hemisphere resulting in a maximum in pressure versus flow. For lower flow rates, the liquid may stream from the meniscus immediately after reaching a hemispherical shape resulting in a plateau in the pressure/flow curve following burst. At the scales considered, the effect of inertia and gravity (and liquid density) are negligible. At sufficiently low flow rates, the meniscus may never reach a hemisphere. Evaporation may balance the flow up the capillary with a lower curvature meniscus, and the maximum pressure may never be reached. More studies are needed to study the influence of the evaporative effects on the capillary pressure across the micro-capillary structure.

[1] For FC-40 and IPA, the meniscus does not become convex at the inner edge of the microcapillary. This is a result of the equilibrium contact angle being reached as soon as the liquid interfaces with the top surface of the microglass capillary.

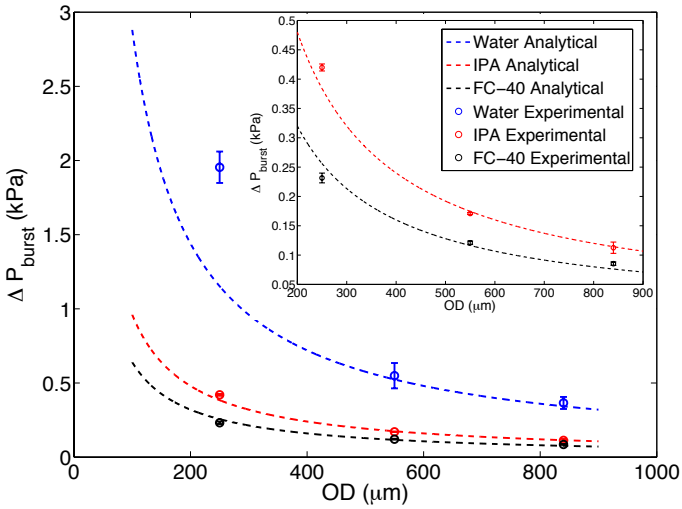

Fig. 12: Trendline comparison of analytical and experimental bursting pressures for glass capillary.

Table 4 summarizes the experimental contributions of the Laplace pressure as a result of the convexity of the meniscus at the outer diameter of the glass capillaries. This result is critical in that our microcooling system will be designed to have a liquid pressure that is greater than the surrounding vapor pressure in order to prevent boiling within the copper microporous layer and utilize evaporative cooling at the bilayer phase separator-vapor interface. Figure 12 is a comparison between the analytical and experimental results. The plot presents the Laplace pressure for different microcapillary OD's for each fluid. The analytical result only captures the pressure due to the outside diameter of the glass tube (OD). However, the experimental result captures the pressures due to both the inner diameter and the outer diameter. Therefore, in order to make a valid comparison, the Young-Laplace pressure due to the inner diameter is subtracted from the experimental result. The rounded edge is approximated to be much less than the outside diameter dimension, r<<d. As expected, the trend shows that the Laplace pressure decreases for an increasing microcapillary OD. The capillary pressure is smallest for FC-40 due to the low surface energy of the fluid. The results for IPA and FC-40 followed the analytical trend well with small uncertainties, <1.0%. For water the uncertainty was found to be ~1-6%. Furthermore, FC-40 and IPA experiments demonstrated more agreement with the model than did the results for water. This can be attributed to significant pinning of water within the glass capillary as it flowed towards the edge of the tube, since water has a lower degree of wettability than FC-40 and IPA. Based on the FC-40 and IPA results, scaling the characteristic dimension down to the 1-0.5 micron range, as would be the case in a realistic membrane for a two-phase device, would yield pressures on the order of 60-130 kPa.

Table 4: Laplace Pressure Across Glass Microcapillaries

OD (μm)	Water (kPa)	IPA (kPa)	FC-40 (kPa)
840	0.365	0.113	0.085
550	0.549	0.171	0.121
250	1.954	0.419	0.427

CONCLUSION

Based on the geometric configuration of alumina membranes, experiments with sizes down to 20 nm, as commercially specified, did not contain adequate bursting pressures as needed for two-phase micro-heat exchanger devices. This paper presents a method for improving the burst pressure characteristics for low surface energy fluids based on the use of sharp, discontinuous geometric configurations. The glass capillary experiments show excellent correspondence with model predictions for the interactions of liquid menisci and sharp geometric features. Experimental evidence, along with model validation, suggests burst pressures in the order of 60-130 kPa, can be achieved with pinning of 1-0.5 μm diameter menisci in dielectric fluids.

The optimization and design of pore geometries is critical for microfluidic cooling applications that utilize dielectric fluids. The results presented in this paper point to opportunities to engineer geometries of surfaces capable of imposing phase separation without burst, even for strongly wetting liquids. Several intrachip/interchip-cooling devices have shifted to the use of dielectric fluids for device compatibility purposes. These devices must rely on two-phase cooling to dissipate such heat. The presented work demonstrates how interchip/interchip-cooling technologies could potentially benefit from such phase-separation implementation

The realization of a microfabricated membrane that exhibits such sharp characteristics is a challenge currently being explored. Future work includes studying bursting pressure at higher fluid temperatures, as is realistic in the two-phase device. Further development on the pore model will account for evaporative effects at the pore edges.

ACKNOWLEDGMENTS

The authors would like to acknowledge financial support from DARPA (agreement # HR0011-13-2-0011, titled: Phase Separation Diamond Microfluidics for HEMT Cooling).

REFERENCES

[1] H. Graeb, "ITRS 2011 analog EDA challenges and approaches," in *Design, Automation & Test in Europe Conference & Exhibition (DATE), 2012*, 2012, pp. 1150-1155.

[2] J. M. Koo, S. Im, L. Jiang, and K. E. Goodson, "Integrated microchannel cooling for three-dimensional electronic circuit architectures," 2005.

[3] M. Farooq, T. Graves-Abe, W. Landers, C. Kothandaraman, B. Himmel, P. Andry*, et al.*, "3D copper TSV integration, testing and reliability," in *Electron Devices Meeting (IEDM), 2011 IEEE International*, 2011, pp. 7.1. 1-7.1. 4.

[4] S.-K. Ryu, K.-H. Lu, T. Jiang, J.-H. Im, R. Huang, and P. S. Ho, "Effect of thermal stresses on carrier mobility and keep-out zone around through-silicon vias for 3-D integration," *Device and Materials Reliability, IEEE Transactions on,* vol. 12, pp. 255-262, 2012.

[5] M. Arik and A. Bar-Cohen, "Immersion cooling of high heat flux microelectronics with dielectric liquids," in *Advanced Packaging Materials, 1998. Proceedings. 1998 4th International Symposium on*, 1998, pp. 229-247.

[6] R. C. Chu, U. P. Hwang, and R. E. Simons, "Conduction Cooling for an LSI Package: A One-Dimensional Approach," *IBM Journal of Research and Development,* vol. 26, pp. 45-54, 1982.

[7] E. G. Colgan, B. Furman, M. Gaynes, W. S. Graham, N. C. LaBianca, J. H. Magerlein*, et al.*, "A practical implementation of silicon microchannel coolers for high power chips," *Components and Packaging Technologies, IEEE Transactions on,* vol. 30, pp. 218-225, 2007.

[8] M. P. David, J. Miler, J. E. Steinbrenner, Y. Yang, M. Touzelbaev, and K. E. Goodson, "Hydraulic and thermal characteristics of a vapor venting two-phase microchannel heat exchanger," *International Journal of Heat and Mass Transfer,* vol. 54, pp. 5504-5516, 12// 2011.

[9] S. Senn and D. Poulikakos, "Laminar mixing, heat transfer and pressure drop in tree-like microchannel nets and their application for thermal management in polymer electrolyte fuel cells," *Journal of Power Sources,* vol. 130, pp. 178-191, 2004.

[10] W. Escher, B. Michel, and D. Poulikakos, "Efficiency of optimized bifurcating tree-like and parallel microchannel networks in the cooling of electronics," *International Journal of Heat and Mass Transfer,* vol. 52, pp. 1421-1430, 2009.

[11] T. Baummer, E. Cetegen, M. Ohadi, and S. Dessiatoun, "Force-fed evaporation and condensation utilizing advanced micro-structured surfaces and micro-channels," *Microelectronics Journal,* vol. 39, pp. 975-980, 2008.

[12] T. W. Kenny, M. Munch, P. Zhou, J. G. Shook, G. Upadhya, K. Goodson*, et al.*, "Method and apparatus for flexible fluid delivery for cooling desired hot spots in a heat producing device," ed: Google Patents, 2006.

[13] T. W. Kenny, M. Munch, P. Zhou, J. G. Shook, G. Upadhya, K. Goodson*, et al.*, "Method and apparatus for efficient vertical fluid delivery for cooling a heat producing device," ed: Google Patents, 2006.

[14] B. Shi, A. Srivastava, and P. Wang, "Non-uniform micro-channel design for stacked 3D-ICs," in *Design Automation Conference (DAC), 2011 48th ACM/EDAC/IEEE*, 2011, pp. 658-663.

[15] L. Zhang, J.-M. Koo, L. Jiang, M. Asheghi, K. E. Goodson, J. G. Santiago*, et al.*, "Measurements and modeling of two-phase flow in microchannels with nearly constant heat flux boundary conditions," *Microelectromechanical Systems, Journal of,* vol. 11, pp. 12-19, 2002.

[16] S. Kumar Saha, G. Piero Celata, and S. G. Kandlikar, "Thermofluid Dynamics of Boiling in Microchannels," in *Advances in Heat Transfer*. vol. Volume 43, I. C. Young and A. G. George, Eds., ed: Elsevier, 2011, pp. 77-226.

[17] L. Lin, A. Pisano, and V. Carey, "Thermal bubble formation on polysilicon micro resistors," *Journal of heat transfer,* vol. 120, pp. 735-742, 1998.

[18] S. Narayanan, A. G. Fedorov, and Y. K. Joshi, "Experimental characterization of a micro-scale thin film evaporative cooling device," in *Thermal and Thermomechanical Phenomena in Electronic Systems (ITherm), 2010 12th IEEE Intersociety Conference on*, 2010, pp. 1-10.

[19] N. Miljkovic, R. Enright, and E. N. Wang, "Effect of droplet morphology on growth dynamics and heat transfer during condensation on superhydrophobic nanostructured surfaces," *Acs Nano,* vol. 6, pp. 1776-1785, 2012.

[20] X. Dai, X. Huang, F. Yang, X. Li, J. Sightler, Y. Yang*, et al.*, "Enhanced nucleate boiling on horizontal hydrophobic-hydrophilic carbon nanotube coatings," *Applied Physics Letters,* vol. 102, p. 161605, 2013.

[21] K. E. Goodson, K. Kurabayashi, and R. F. W. Pease, "Improved heat sinking for laser-diode arrays using microchannels in CVD diamond," *Components, Packaging, and Manufacturing Technology, Part B: Advanced Packaging, IEEE Transactions on,* vol. 20, pp. 104-109, 1997.

[22] E. N. Wang, R. Xiao, and K.-H. Chu, "Nanoengineered surfaces for microfluidic-based thermal management devices," in *Proceedings of SPIE*, 2010, p. 759202.

[23] V. P. Carey, *Liquid-Vapor Phase-Change Phenomena: An Introduction to the Thermophysics of Vaporization and Condensation Processes in Heat Transfer Equipment*: Taylor & Francis Group, 2008.

[24] M. P. David, J. E. Steinbrenner, J. Miler, and K. E. Goodson, "Adiabatic and diabatic two-phase venting flow in a microchannel," *International Journal of Multiphase Flow,* vol. 37, pp. 1135-1146, 11// 2011.

[25] D. Quéré, "Wetting and roughness," *Annu. Rev. Mater. Res.,* vol. 38, pp. 71-99, 2008.

[26] J. Oliver, C. Huh, and S. Mason, "Resistance to spreading of liquids by sharp edges," *Journal of Colloid and Interface Science,* vol. 59, pp. 568-581, 1977.

[27] Y. Mori, T. Van de Ven, and S. Mason, "Resistance to spreading of liquids by sharp edged microsteps," *Colloids and Surfaces,* vol. 4, pp. 1-15, 1982.

[28] P. S. Forsberg, C. Priest, M. Brinkmann, R. Sedev, and J. Ralston, "Contact line pinning on microstructured

surfaces for liquids in the Wenzel state," *Langmuir,* vol. 26, pp. 860-865, 2009.
[29] Y. Su, B. Ji, K. Zhang, H. Gao, Y. Huang, and K. Hwang, "Nano to micro structural hierarchy is crucial for stable superhydrophobic and water-repellent surfaces," *Langmuir,* vol. 26, pp. 4984-4989, 2010.
[30] L. Cao, H.-H. Hu, and D. Gao, "Design and fabrication of micro-textures for inducing a superhydrophobic behavior on hydrophilic materials," *Langmuir,* vol. 23, pp. 4310-4314, 2007.
[31] W. Choi, A. Tuteja, S. Chhatre, J. M. Mabry, R. E. Cohen, and G. H. McKinley, "Fabrics with tunable oleophobicity," *Advanced Materials,* vol. 21, pp. 2190-2195, 2009.
[32] A. Tuteja, W. Choi, G. H. McKinley, R. E. Cohen, and M. F. Rubner, "Design parameters for superhydrophobicity and superoleophobicity," *MRS bulletin,* vol. 33, pp. 752-758, 2008.
[33] A. K. Kota, J. M. Mabry, and A. Tuteja. (2013, Superoleophobic surfaces: design criteria and recent studies. *Surface Innovations 1,* 71-83.
[34] A. Ahuja, J. A. Taylor, V. Lifton, A. A. Sidorenko, T. R. Salamon, E. J. Lobaton*, et al.*, "Nanonails: A Simple Geometrical Approach to Electrically Tunable Superlyophobic Surfaces," *Langmuir,* vol. 24, pp. 9-14, 2008/01/01 2007.
[35] A. Gliere and C. Delattre, "Modeling and fabrication of capillary stop valves for planar microfluidic systems," *Sensors and Actuators A: Physical,* vol. 130, pp. 601-608, 2006.
[36] H. Cho, H.-Y. Kim, J. Y. Kang, and T. S. Kim, "How the capillary burst microvalve works," *Journal of colloid and interface science,* vol. 306, pp. 379-385, 2007.
[37] M. G. Hospital, "Capillary Flow," pp. 192-197, 2005.
[38] M. Zimmermann, P. Hunziker, and E. Delamarche, "Valves for autonomous capillary systems," *Microfluidics and Nanofluidics,* vol. 5, pp. 395-402, 2008.
[39] J. Berthier, F. Loe-Mie, V.-M. Tran, S. Schoumacker, F. Mittler, G. Marchand*, et al.*, "On the pinning of interfaces on micropillar edges," *Journal of colloid and interface science,* vol. 338, pp. 296-303, 2009.
[40] J. Berthier, V.-M. Tran, F. Mittler, and N. Sarrut, "The physics of a coflow micro-extractor: interface stability and optimal extraction length," *Sensors and Actuators A: Physical,* vol. 149, pp. 56-64, 2009.
[41] W. Tong, A. Bar-Cohen, T. W. Simon, and S. M. You, "Contact angle effects on boiling incipience of highly-wetting liquids," *International Journal of Heat and Mass Transfer,* vol. 33, pp. 91-103, 1// 1990.
[42] R. Redón, A. Vázquez-Olmos, M. E. Mata-Zamora, A. Ordóñez-Medrano, F. Rivera-Torres, and J. M. Saniger, "Contact angle studies on anodic porous alumina," *Journal of Colloid and Interface Science,* vol. 287, pp. 664-670, 7/15/ 2005.